Testing general relativity using higher-order modes of gravitational waves from binary black holes

Anna Puecher[1,2] Chinmay Kalaghatgi[1,2,3] Soumen Roy,[1,2] Yoshinta Setyawati[1,2] Ish Gupta,[4]
B. S. Sathyaprakash[4,5,6] and Chris Van Den Broeck[1,2]

[1]*Nikhef—National Institute for Subatomic Physics, Science Park 105, 1098 XG Amsterdam, Netherlands*
[2]*Institute for Gravitational and Subatomic Physics (GRASP), Utrecht University,
Princetonplein 1, 3584 CC Utrecht, Netherlands*
[3]*Institute for High-Energy Physics, University of Amsterdam,
Science Park 904, 1098 XH Amsterdam, Netherlands*
[4]*Institute for Gravitation and the Cosmos, Department of Physics, Penn State University,
University Park, Pennsylvania 16802, USA*
[5]*Department of Astronomy and Astrophysics, Penn State University,
University Park, Pennsylvania 16802, USA*
[6]*School of Physics and Astronomy, Cardiff University,
Cardiff CF24 3AA, United Kingdom*

Recently, strong evidence was found for the presence of higher-order modes in the gravitational wave signals GW190412 and GW190814, which originated from compact binary coalescences with significantly asymmetric component masses. This has opened up the possibility of new tests of general relativity by looking at the way in which the higher-order modes are related to the basic signal. Here we further develop a test which assesses whether the amplitudes of subdominant harmonics are consistent with what is predicted by general relativity. To this end we incorporate a state-of-the-art waveform model with higher-order modes and precessing spins into a Bayesian parameter estimation and model selection framework. The analysis methodology is tested extensively through simulations. We investigate to what extent deviations in the relative amplitudes of the harmonics will be measurable depending on the properties of the source, and we map out correlations between our testing parameters and the inclination of the source with respect to the observer. Finally, we apply the test to GW190412 and GW190814, finding no evidence for violations of general relativity.

I. INTRODUCTION

The Advanced LIGO [1] and Advanced Virgo [2] gravitational wave (GW) observatories have by now detected 90 candidate signals from coalescing binary black holes [3–8], binary neutron stars [9,10], and neutron star–black hole systems [11]. A battery of tests of general relativity (GR) were performed [12–17], including tests of the spacetime dynamics as inferred from the binary coalescence process [18–24].

Recently, strong evidence was obtained for the presence of higher-order modes [25] in the gravitational wave signals GW190412 and GW190814 [26–28], which were emitted by coalescing binary compact objects with significantly different component masses. Measuring these sub-dominant harmonics of the basic signal enables more precise measurements of the source parameters, and can allow for stronger constraints on certain deviations from GR [29,30]. Several tests of GR that directly probe the harmonic structure for binary black hole (BBH)

coalescences[1] were proposed in [33–36]. These fall into two categories. In the first case, one tests the phase evolution, e.g., by testing for deviations in the way parameters like the chirp mass and symmetric mass ratio enter into the expressions for the different harmonics [33]. This kind of test has already been applied to GW190412 and GW190814 in Ref. [37]. A second test looks for anomalies in the amplitudes of the subdominant modes [34]; the latter test is the focus of this paper.

Specifically, defining $h(t) \equiv h_+(t) - i h_\times(t)$ with h_+, $h_\times$ the two polarizations, the GW signal from a coalescing binary can be written as

---

[1]Given the low mass of the lighter component of GW190814 ($\simeq 2.6\ M_\odot$), there is a possibility that it was a signal from a neutron star-black hole rather than a binary black hole coalescence [27], but studies based on the known properties of neutron stars make a BBH origin much more likely [31,32]. For the purposes of this paper we will assume that GW190814 came from a BBH coalescence.

$$h(t; \iota, \phi_0, \vec{\lambda}) = \sum_{\ell=2}^{\infty} \sum_{m=-\ell}^{\ell} Y_{-2}^{\ell m}(\iota, \phi_0) h_{\ell m}(t; \vec{\lambda}), \quad (1)$$

where the $Y_{-2}^{\ell m}$ are spin-weighted spherical harmonics of weight -2, (ι, ϕ_0) indicate the direction of the radiation in the source frame, and $\vec{\lambda}$ collects all other parameters in the problem. The latter are the total mass $M \equiv m_1 + m_2$ (with m_1, m_2 the component masses), the mass ratio $q \equiv m_1/m_2$ (where we assume $m_1 \geq m_2$), the dimensionless spin vectors $\mathbf{S}_1$ and $\mathbf{S}_2$ at some reference time t_{ref}, a reference phase φ_{ref}, and the luminosity distance D_{L}. The $h_{\ell m}$ will be referred to as the "modes" of the gravitational wave signal. Taking the contribution with $\ell = 2$, $m = \pm 2$ to constitute the fundamental mode, the test of GR considered here follows Ref. [34] to allow for deviations in the amplitudes of the higher-order modes:

$$\begin{aligned} h(t; \iota, \phi_0, \vec{\lambda}) &= \sum_{m=\pm 2} Y_{-2}^{2m}(\iota, \phi_0) h_{2m}(t; \vec{\lambda}) \\ &+ \sum_{\text{HOM}} \sum_{m=-\ell}^{\ell} (1 + c_{\ell m}) Y_{-2}^{\ell m}(\iota, \phi_0) h_{\ell m}(t; \vec{\lambda}), \end{aligned}$$
$$(2)$$

where HOM stands for the ℓ labels of the higher-order modes. The $c_{\ell m}$ are free parameters, to be measured together with all other parameters in the problem; the case where GR is valid corresponds to $c_{\ell m} = 0$. Although for precessing signals one does not have the symmetry $h_{\ell-m} = (-1)^\ell h_{\ell m}^*$ [38], for definiteness we set $c_{\ell-m} = c_{\ell m}$. Here we will perform parametrized tests where the $c_{\ell|m|}$ are allowed to vary one by one, as in the phase-based tests performed in [12–16], and we will focus on modes that will usually be the strongest, namely the ones with $(\ell, |m|) = (3, 3)$ and $(\ell, |m|) = (2, 1)$. We will not only perform parameter estimation, as was done in Ref. [34], but also model selection; as we shall see, the latter will be of particular importance here.

To leading order, the observed strengths of the higher harmonics are set by the total mass M, the inclination angle ι, and the relative mass difference $\Delta \equiv (m_1 - m_2)/M$ [25,39]. One aim of this paper is to investigate to what extent deviations in amplitudes of the harmonics can be determined depending on the values of these parameters, in terms of both parameter estimation and model selection. Second, when performing tests that allow for nonzero $c_{\ell m}$, there will be correlations between these and the angular parameters, notably ι, which will affect both the measurability of the deviations from GR and the shapes of the posterior distributions. We will map out this interplay, which is necessary to interpret the results of our tests. Finally, for the first time we apply this test to GW190412 and GW190814.

The rest of this paper is structured as follows. In Sec. II we recall the basic properties of higher harmonics, together with the waveform model we will use. In Sec. III we set up the Bayesian analysis framework used in this study, and explain our choices for simulated signals (or injections), which will be used to understand the behavior of our analysis depending on the properties of the GW source. Section IV shows the results of our simulations and of measurements on GW190412 and GW190814. A summary and conclusions are provided in Sec. V.

II. PROPERTIES OF HIGHER HARMONICS AND WAVEFORM MODEL

Let us start by recalling some properties of the harmonics $h_{\ell m}$ in Eq. (1), which we will need to interpret the results in subsequent sections. In doing so we limit ourselves to qualitative statements, mostly referring to the inspiral regime; for explicit dependences on the parameters in the problem we refer to Refs. [25,39]. The salient features relevant to us here are as follows:

(i) At zeroth post-Newtonian order (0PN) in amplitude there is the harmonic with $\ell = |m| = 2$, which is the most dominant of all multipole modes.

(ii) At 0.5PN order in amplitude, harmonics with $(\ell, |m|) = (2, 1), (3, 3), (3, 1)$ appear. In this paper we will be the most interested in the $(2, 1)$ and $(3, 3)$ harmonics, since the $(3, 1)$ harmonic is suppressed with respect to the others due to its small overall numerical prefactor. For purposes of testing GR we will also not consider harmonics that only appear at higher PN order.

(iii) The $(2, 1)$ and $(3, 3)$ modes are proportional to the relative mass difference $\Delta = (m_1 - m_2)/M$, so that they are more prominent for systems with a higher value of $q = m_1/m_2$.

(iv) The fact that the harmonics enter the polarizations through the spin-weighted spherical harmonics $Y_{-2}^{\ell m}(\iota, \phi_0)$ causes their prominence to depend sensitively on the inclination angle ι, as illustrated in Fig. 1. For systems that are "face-on" ($\iota = 0$) or "face-off" ($\iota = 180°$), only the dominant harmonic is visible. The subdominant harmonics on which we will focus in this work are strongest around $\iota \simeq 50°$ and $\iota \simeq 130°$. In the figure we also indicate the peak likelihood values of ι for GW190412 and GW190814.

(v) Finally, the observed power in the subdominant modes relative to that in the $(2, 2)$ mode increases with the total mass. During inspiral, at a given frequency f the ratios of the subdominant mode amplitudes to that of the dominant one grow with M through powers of $(Mf)^{1/3}$, though also the merger part of the signal and the shape of the noise power spectral density $S_n(f)$ will have an effect.
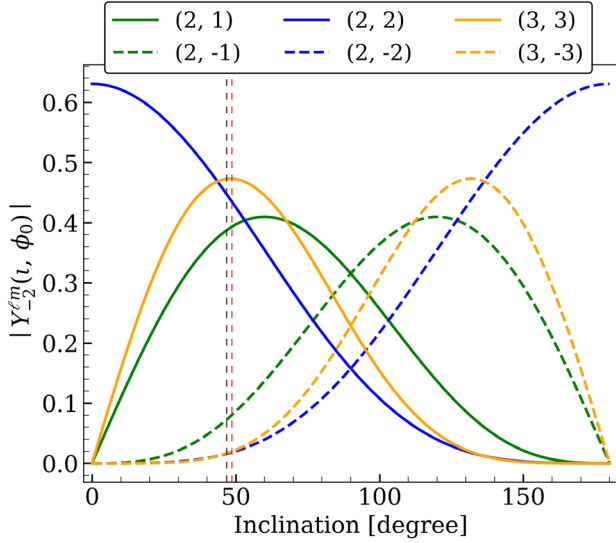
FIG. 1. The absolute values of spin-weighted spherical harmonics of weight -2 as function of the inclination angle ι. The vertical lines indicate the peak likelihood values of ι for GW190412 (black dashed) and GW190814 (red dashed), located at $\simeq 47°$ and $\simeq 49°$, respectively [26,27].

FIG. 2. The relative signal power in the real part of $h_{\ell m}$ for some of the higher-order modes with respect to the dominant (2, 2) mode, as a function of the total mass M of the binary, for three different values of the mass ratio q and assuming Advanced LIGO at design sensitivity.

To make the latter point more concrete, let us define the quantities

$$\alpha_{\ell m} \equiv \int_{f_{\text{low}}}^{f_{\text{high}}} \frac{|\tilde{h}_{\ell m}(f; \vec{\lambda})|^2}{S_n(f)} df \Big/ \int_{f_{\text{low}}}^{f_{\text{high}}} \frac{|\tilde{h}_{22}(f; \vec{\lambda})|^2}{S_n(f)} df, \qquad (3)$$

where $\tilde{h}_{\ell m}(f; \vec{\lambda})$ is the (ℓ, m) mode in the frequency domain, and $S_n(f)$ denotes the one-sided detector noise power spectral density, which we take to be the one for Advanced LIGO at design sensitivity [1]. The integrals are evaluated from a lower cutoff frequency $f_{\text{low}} = 20$ Hz to an upper cutoff frequency $f_{\text{high}} = 2048$ Hz, which amply suffices for the kinds of signals considered in this paper. The waveform model is taken to be the most up-to-date phenomenological inspiral-merger-ringdown model IMRPhenomXPHM [40,41], which incorporates harmonics with $(\ell, |m|) = (2, 2), (2, 1), (3, 3), (3, 2), (4, 4)$ modes, as well as effects of spin-induced precession. Figure 2 shows the dependence of the $\alpha_{\ell m}$ on total mass M and mass ratio q, for $(\ell, m) = (2, 1), (3, 3)$, where for simplicity we have focused on binaries composed of nonspinning black holes. Note that $q = 3, 6, 9$ correspond to $\Delta \simeq 0.5, 0.71, 0.8$, respectively, which explains why the curves with $q = 6, 9$ are closer to each other than to the ones for $q = 3$.

III. ANALYSIS FRAMEWORK AND SETUP OF SIMULATIONS

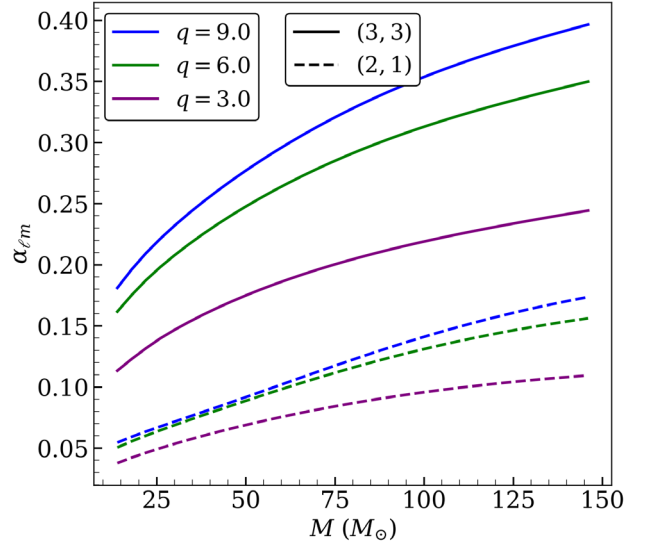We now explain our data analysis methodology for measuring source parameters and to rank hypotheses based on the available detector data. Next we will detail the choices made for simulations that were performed to understand the response of the analysis framework to possible violations of GR in the amplitudes of different harmonics.

A. Analysis framework

Consider detector data d and a hypothesis $\mathcal{H}$, where, for practical purposes, the latter corresponds to a waveform model $\tilde{h}(f; \vec{\theta})$; in our case this could be the GR model for binary black hole coalescence, or one that allows for deviations from GR in the amplitudes of one of the harmonics. Then, in a Bayesian setting, measuring the parameters $\vec{\theta}$ of the source amounts to obtaining the *posterior probability density* $p(\vec{\theta}|d, \mathcal{H})$. From Bayes's theorem,

$$p(\vec{\theta}|d, \mathcal{H}) = \frac{p(d|\vec{\theta}, \mathcal{H})p(\vec{\theta}|\mathcal{H})}{p(d|\mathcal{H})}, \qquad (4)$$

where the *evidence* $p(d|\mathcal{H})$ for the hypothesis $\mathcal{H}$ is given by

$$p(d|\mathcal{H}) = \int d\vec{\theta} p(d|\vec{\theta}, \mathcal{H})p(\vec{\theta}|\mathcal{H}). \qquad (5)$$

In the above, $p(\vec{\theta}|\mathcal{H})$ is the *prior probability density*, and the *likelihood* $p(d|\vec{\theta}, \mathcal{H})$ takes the form [42]

$$p(d|\vec{\theta}, \mathcal{H}) \propto \exp\left[-\frac{1}{2}\langle d - h(\vec{\theta})|d - h(\vec{\theta})\rangle\right], \qquad (6)$$

where the noise-weighted inner product $\langle\cdot|\cdot\rangle$ is given by

$$\langle a|b\rangle \equiv 4\,\mathrm{Re}\int_{f_{\mathrm{low}}}^{f_{\mathrm{high}}}\frac{\tilde{a}^*(f)\tilde{b}(f)}{S_n(f)}\,df. \quad (7)$$

Equation (4) together with Eqs. (5)–(7) allow us to calculate the posterior probability density $p(\vec{\theta}|d,\mathcal{H})$ from the data. The posterior probability density $p(\theta_k|d,\mathcal{H})$ for a particular parameter in $\vec{\theta}$ is obtained by integrating out all the other parameters $\vec{\xi}$ in $\vec{\theta}=(\theta_k,\vec{\xi})$:

$$p(\theta_k|d,\mathcal{H}) = \int d\vec{\xi}\,p(\theta_k,\vec{\xi}|d,\mathcal{H}). \quad (8)$$

Additionally, we will want to rank hypotheses: the GR hypothesis $\mathcal{H}_{\mathrm{GR}}$ versus hypotheses $\mathcal{H}_{\mathrm{NonGR}}$, which allow one of the $c_{\ell m}$ in Eq. (2) to be nonzero. To this end we calculate *Bayes factors*, or ratios of evidences,

$$\mathcal{B}_{\mathrm{GR}}^{\mathrm{NonGR}} \equiv \frac{p(d|\mathcal{H}_{\mathrm{NonGR}})}{p(d|\mathcal{H}_{\mathrm{GR}})}, \quad (9)$$

where $p(d|\mathcal{H}_{\mathrm{NonGR}})$ and $p(d|\mathcal{H}_{\mathrm{GR}})$ are obtained using Eq. (5), taking $\mathcal{H}$ to be $\mathcal{H}_{\mathrm{NonGR}}$ or $\mathcal{H}_{\mathrm{GR}}$, respectively. In practice it is usually convenient to focus on the logarithm of the Bayes factor, $\ln\mathcal{B}_{\mathrm{GR}}^{\mathrm{NonGR}}$, as will also be done here. To interpret the size of (log) Bayes factors, one could make use of the Jeffreys scale [43], in which $\mathcal{B}_{\mathrm{GR}}^{\mathrm{NonGR}} > 10^2$ (or $\ln\mathcal{B}_{\mathrm{GR}}^{\mathrm{NonGR}} \gtrsim 4.6$) would be deemed a "decisive" grade of evidence. Alternatively one could construct a background distribution for $\ln\mathcal{B}_{\mathrm{GR}}^{\mathrm{NonGR}}$ from a large number of injections that are in accordance to GR (see e.g., [21]), though this is computationally costly. Here we mainly want to show trends; a more extensive treatment of (log) Bayes factors is left for future work.

It will also be important to consider the loudness of a signal as it appears in a detector. The optimal *signal-to-noise ratio* (SNR) is defined as $\rho \equiv \langle h(\vec{\theta})|h(\vec{\theta})\rangle^{1/2}$. For a network of detectors, the combined optimal SNR is obtained by summing in quadrature the SNRs in the individual detectors.

Finally, for estimating the evidence integrals as in Eq. (5), and obtaining samples for posterior density distributions $p(\vec{\theta}|d,\mathcal{H})$, we used nested sampling [42,44] as implemented in the LALinference package [45] of the LIGO Algorithms Library software suite [46]. Both for simulated signals and for template waveforms we use IMRPhenomXPHM, with testing parameters $c_{\ell m}$ added as in Eq. (2) in the case of non-GR waveforms. For the purpose of our analyses, the free parameters are then the usual ones that enter a binary black hole signal, together with one of the $c_{\ell m}$ in the case of a non-GR hypothesis. The posterior density distribution for a $c_{\ell m}$ by itself is obtained

from the joint posterior distribution by integrating out all other parameters, as in Eq. (8).

B. Setup of the simulations

To understand the response of our analysis pipeline to GR violations in mode amplitudes with various strengths, we add simulated signals, or injections, to synthetic stationary, Gaussian noise for a network of Advanced LIGO and Virgo detectors following the predicted noise spectral densities at design sensitivity [1,2]. Since higher-order modes are more prominent for larger total masses, we will start by considering heavier BBH systems. Later in the paper we will analyze the real GW events GW190412 and GW190814 to look for GR violations. To this end, for lower-mass systems we will perform injections whose GR parameter values and SNRs are set to the maximum-likelihood values obtained from analyses on these events that assumed GR to be correct. Specifically:

  (i) We will inject signals with $M = 65\,M_\odot$ and $M = 120\,M_\odot$, for mass ratios $q = 3$, 6, 9. Here the inclination angle is fixed to be $\iota = 45°$, and the network SNR to 25. For simplicity, in these injections we set the spins to zero, although throughout this paper the analyses allow for nonzero, precessing spins.

 (ii) For GW190412-like injections, $M = 46.6\,M_\odot$, $q = 4.2$, $\iota = 47°$. Spin-related and other parameters are set to their maximum-likelihood values for the real event [26], so that in particular these injections have precessing spins. The network SNR is 19.8.

(iii) For GW190814-like injections, $M = 27.6\,M_\odot$, $q = 9.3$, $\iota = 49°$; here too all parameters are set to the maximum-likelihood ones [27]. The network SNR is 25.

We also need to choose values for the deviation parameters c_{33} and c_{21} in the injections. Since the (3, 3) mode will tend to be the strongest (see Fig. 2), we can expect smaller values of c_{33} to lead to detectable GR violations than for c_{21}, where "detectable" can be taken to mean that the 90% credible region of the posterior density function has support that excludes zero. We found that, at least for the higher masses listed above, the following choices constitute examples ranging from nondetectability to easy detectability of the GR violations:

  (i) $c_{33} = 0.5$, 1.5, 3.

 (ii) $c_{21} = 1$, 3, 6.

Hence these are the values for which we will show results in the next section.

IV. RESULTS OF SIMULATIONS, AND ANALYSES OF GW190412 AND GW190814

We now describe the results for our simulations, as well as for the real events GW190412 and GW190814, in terms of parameter estimation and hypothesis ranking. In doing
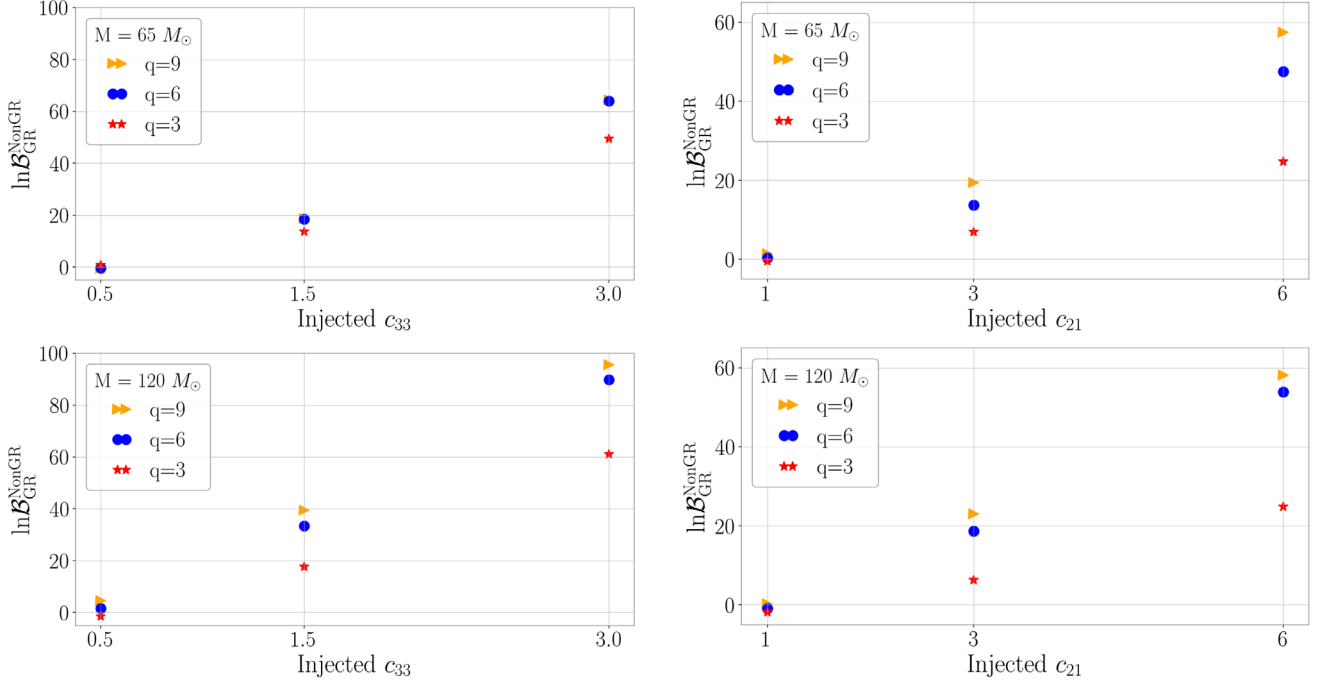
FIG. 3. $\ln \mathcal{B}_{\rm GR}^{\rm NonGR}$ for $M = 65\,M_{\odot}$ (top row) and $M = 120\,M_{\odot}$ (bottom row), for different mass ratios q indicated by the differently shaped markers. The horizontal axes show the injected values of c_{33} (left column) and c_{21} (right column). In each case, the non-GR hypothesis has the corresponding $c_{\ell m}$ as free parameter.

so, it will be useful to make a distinction between the more massive BBHs ($M = 65, 120\,M_{\odot}$), the injections with parameters similar to those of the real events, and of course the real events themselves.

A. More massive binary black holes

Let us first look at results for injections with $M = 65\,M_{\odot}$ and $M = 120\,M_{\odot}$. To have an easier overview it is convenient to first look at the behavior of log Bayes factors, $\ln \mathcal{B}_{\rm GR}^{\rm NonGR}$, which we do in Fig. 3. The trends are as follows:

(1) As expected, for a larger injected $c_{\ell m}$, the log Bayes factor is larger. The cases $c_{33} = 0.5$ and $c_{21} = 1$ lead to $\ln \mathcal{B}_{\rm GR}^{\rm NonGR}$ that tend to be consistent with zero, meaning that the data are not sufficiently informative to clearly distinguish between hypotheses. However, starting from $c_{33} = 1.5$ or $c_{21} = 3$, the $\ln \mathcal{B}_{\rm GR}^{\rm NonGR}$ are significantly away from zero, and as will be seen in terms of parameter estimation below, here the GR deviations tend to be detectable.

(2) Higher values of M lead to higher $\ln \mathcal{B}_{\rm GR}^{\rm NonGR}$, consistent with there being more power in the higher-order modes relative to the (2, 2) mode; see Fig. 2.

(3) Again as expected, on the whole a larger mass ratio q tends to lead to a higher $\ln \mathcal{B}_{\rm GR}^{\rm NonGR}$, consistent with there being more power in the higher-order modes. We do see that the $\ln \mathcal{B}_{\rm GR}^{\rm NonGR}$ tend to differ less between $q = 6$ and $q = 9$ than between $q = 3$ and $q = 6$; in fact, for $M = 65\,M_{\odot}$ and c_{33}, the log

Bayes factors for the higher two values of q are nearly equal. Again pointing to Fig. 2, we note that the cases $q = 6$ and $q = 9$ are closer to each other than to $q = 3$ in terms of the power present in higher-order modes.

Figure 4 shows posterior probability densities for the corresponding injections. The trends show broad consistency with what we saw for the log Bayes factors. In particular, for the injected values $c_{33} = 0.5$ and $c_{21} = 1$, posterior densities either include the GR value of zero, or extend to quite close to it, while for higher injected values, the GR value tends to be outside the support of the distribution. Also, the 90% confidence intervals tend to be tighter for higher total mass and for higher mass ratio, again consistent with the behavior of the $\ln \mathcal{B}_{\rm GR}^{\rm NonGR}$ in Fig. 3, and indeed with Fig. 2.

B. Injections with parameters similar to those of GW190412 and GW190814

Next we turn to injections with GR parameters close to those of the real events GW190412 and GW190814. Figure 5 shows results for $\ln \mathcal{B}_{\rm GR}^{\rm NonGR}$. Here too the trends are as expected: the log Bayes factor increases with increasing injected values for c_{33} and c_{21}. Note that although GW190412 had a higher mass than GW190814 ($M = 46.6\,M_{\odot}$ versus $M = 27.6\,M_{\odot}$), the mass ratio of GW190412 was considerably smaller than that of GW190814 ($q = 4.2$ versus $q = 9.3$). The log Bayes factors are higher for the latter event, consistent with
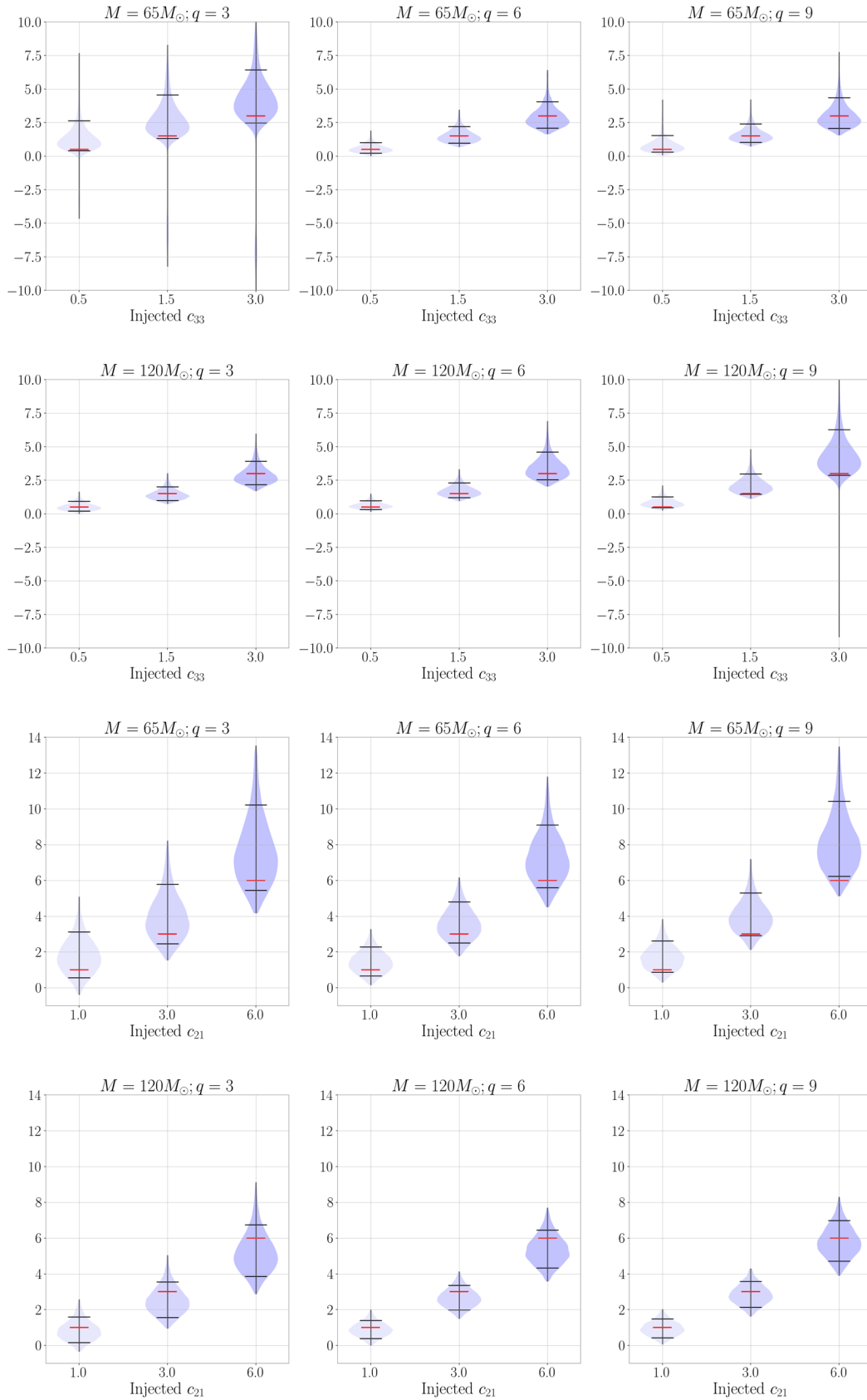
FIG. 4.   Violin plots for the posterior density distributions of c_{33} (top two rows) and c_{21} (bottom two rows), for $M = 65, 120 \, M_\odot$, and $q = 3$ (left column), $q = 6$ (middle column), and $q = 9$ (right column). In each case the black horizontal bars indicate 90% confidence intervals, and the red horizontal bar the injected value; the black vertical line shows the support of the posterior.
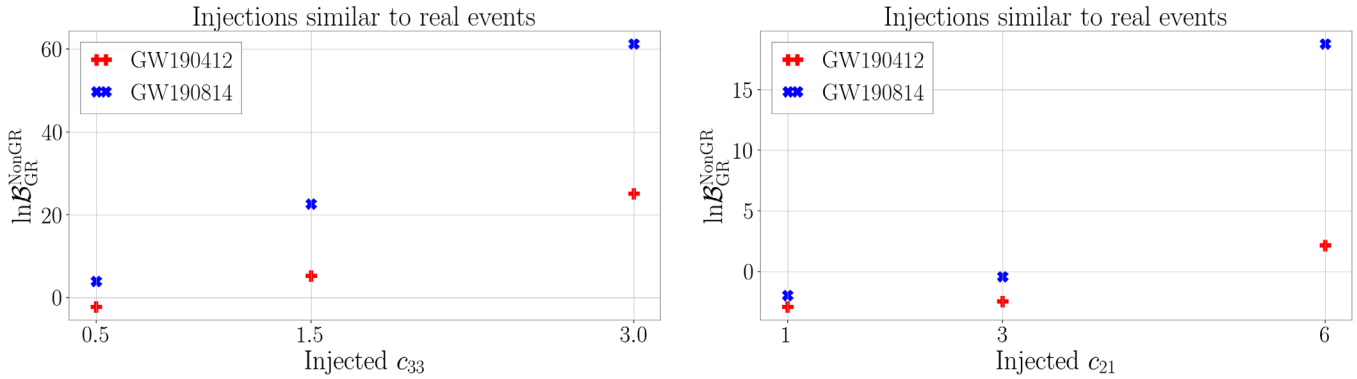
FIG. 5. $\ln \mathcal{B}_{\mathrm{GR}}^{\mathrm{NonGR}}$ for injections with GR parameters similar to those of GW190412 and GW190814.

Fig. 2. We see that for GW190412 one has $\ln \mathcal{B}_{\mathrm{GR}}^{\mathrm{NonGR}} < 0$ for $c_{33} = 0.5$, and the same is true for both injections in the cases $c_{21} = 1$ and $c_{21} = 3$, presumably due to the lower total masses. We note that uncertainties on log Bayes factors can be expected to be of $\mathcal{O}(\mathrm{few})$ [42]. Hence the small negative values can be interpreted as being consistent with zero, and the $\ln \mathcal{B}_{\mathrm{GR}}^{\mathrm{NonGR}}$ are uninformative in these cases.

Figure 6 shows posterior probability distributions for the same injections. In all cases, the injected value for c_{33} and c_{21} lies within the support of the posterior. For c_{21} the results look like what one might expect, but for c_{33} the posteriors are bimodal, with the true value not always lying in the strongest mode. As will be clarified in the next section, this behavior results from a partial degeneracy between c_{33} and the inclination angle ι.
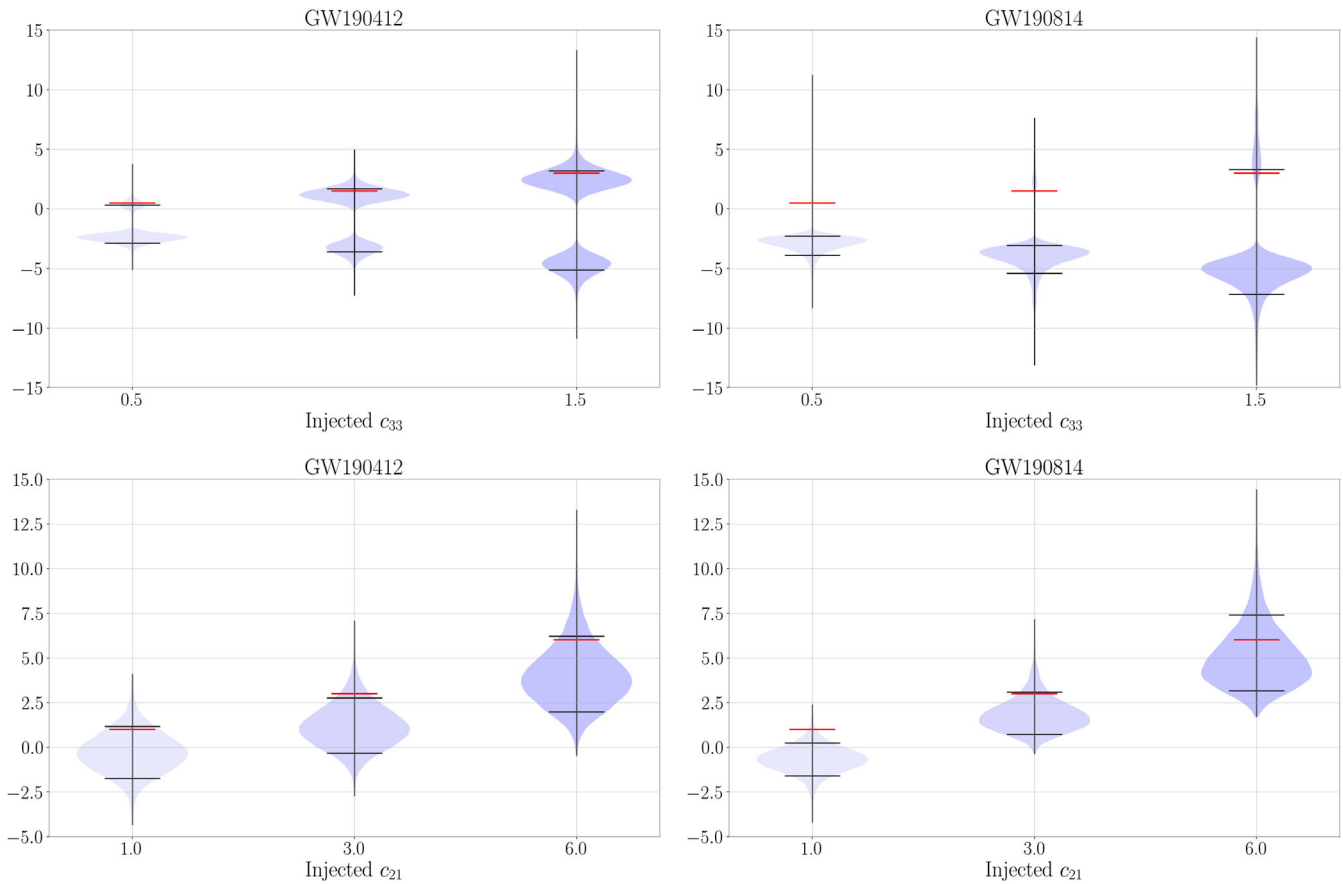

FIG. 6.   Violin plots for the posterior density distributions of c_{33} (top row) and c_{21} (bottom row), for injections similar to GW190412 (left column) and GW190814 (right column). In each case the black horizontal bars indicate 90% confidence intervals, and the red horizontal bar the injected value; the black vertical line shows the support of the posterior.

TABLE I. Values of $\ln \mathcal{B}_{\mathrm{GR}}^{\mathrm{NonGR}}$ for analyses of the real events GW190412 and GW190814.

Event	GW190412	GW190814
c_{33}	−1.25	−3.96
c_{21}	−2.48	−1.77

C. Results for GW190412 and GW190814

Finally we turn to the real events GW190412 and GW190814. Table I shows the results for $\ln \mathcal{B}_{\mathrm{GR}}^{\mathrm{NonGR}}$ when comparing the hypothesis of a nonzero c_{33} or c_{21} with the GR hypothesis. All the log Bayes factors are negative, so we have no reason to suspect a violation of GR in the amplitudes of subdominant modes.

More interesting are the posterior distributions for c_{21} and especially c_{33}, which are shown in Figs. 7 and 8. For both events, the posterior for c_{21} is unimodal, and consistent with the GR value of zero. However, just like in the simulations of the previous section, the posterior for c_{33} is bimodal, also for both events.

As it turns out, this bimodality results from a degeneracy between c_{33} and the inclination angle ι. The lower panels of Figs. 7 and 8 show *mismatches* between (1) a reference waveform $\tilde{h}_{\mathrm{ref}}(f)$, which is a GR waveform with maximum-likelihood parameters for the respective signals, and (2) a waveform $\tilde{h}(c_{\ell m}, \iota; f)$ in which $c_{\ell m}$ and ι can take on arbitrary values, but all other parameters are the maximum-likelihood ones from the GR analysis. Specifically, we compute

$$\mathrm{MM} = 1 - \max_{t_0, \varphi_0} \frac{\langle h_{\mathrm{ref}} | h(c_{\ell m}, \iota) \rangle}{\sqrt{\langle h_{\mathrm{ref}} | h_{\mathrm{ref}} \rangle} \sqrt{\langle h(c_{\ell m}, \iota) | h(c_{\ell m}, \iota) \rangle}}, \quad (10)$$

where the maximization is over a rigid time shift and overall phase.

In the bottom panels of Figs. 7 and 8, these mismatches are indicated with color coding, with dark colors signifying small mismatch. Overlaid are dashed lines indicating the peak-likelihood values in the (bimodal) posterior distribution for ι obtained when analyzing the events with either c_{21} or c_{33} as additional free parameters. Focusing first on the case of c_{33} and GW190412 in Fig. 7, we see that there are two regions in the (c_{33}, ι) plane where mismatches are low: one region that contains the GR value $c_{33} = 0$ and is consistent with the lower value of ι, and another region consistent with the higher ι value and $c_{33} \neq 0$. In either region, waveforms $h(c_{33}, \iota)$ are consistent with the reference waveform h_{ref}, which explains the bimodality in the posterior for c_{33}. By contrast, based on the analogous plot
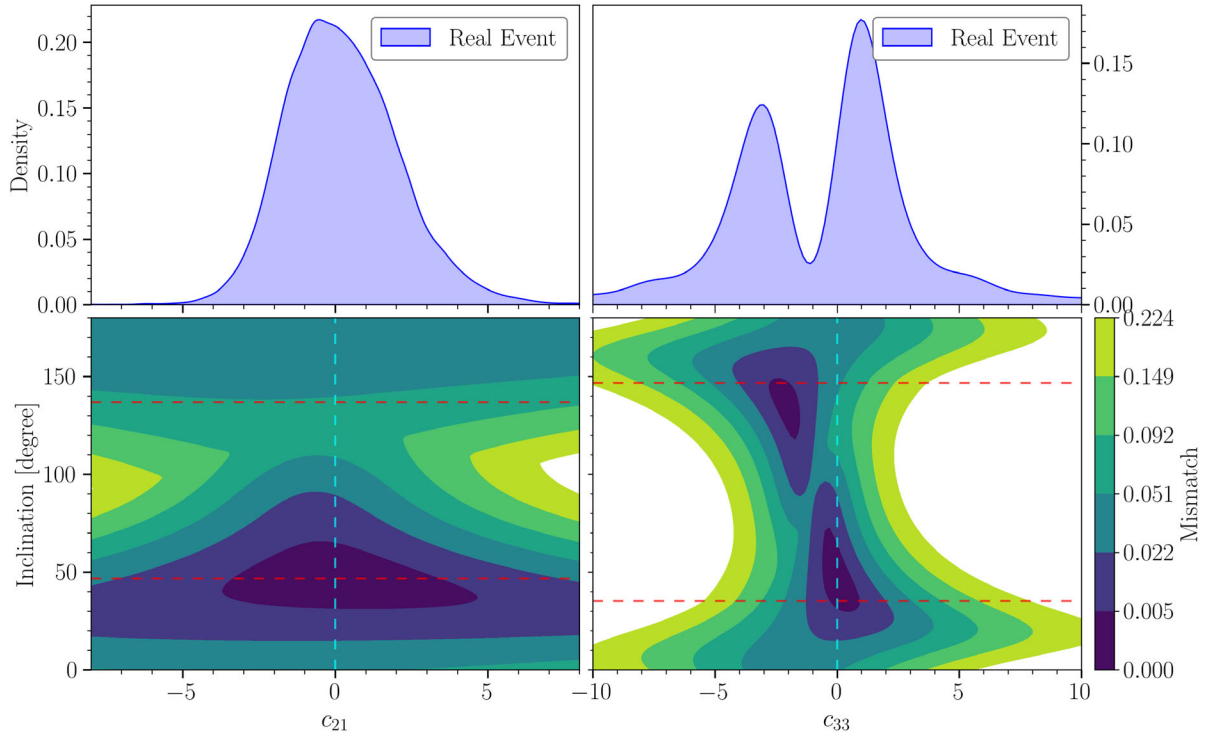

FIG. 7. Top panels: posterior density functions for c_{21} (left) and c_{33} (right) for GW190412. Bottom panels: contours of constant mismatch between the maximum-likelihood GR waveform, and a waveform in which ι and c_{21} (left) or c_{33} (right) are varied while keeping all other parameters the same. The dashed vertical lines indicate the GR values $c_{21} = 0$ and $c_{33} = 0$, respectively, and the dashed horizontal lines indicate the peak-likelihood values for ι obtained from the analyses of GW190412 with respectively c_{21} and c_{33} as free parameters.
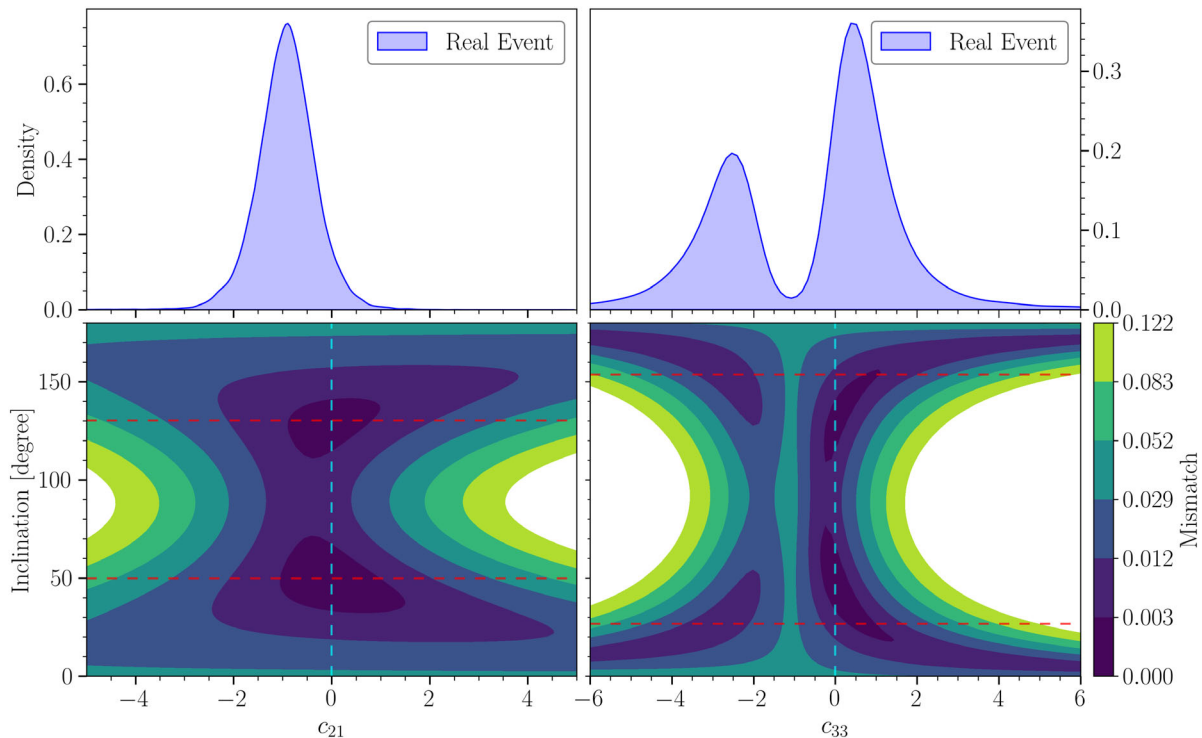
FIG. 8.　The same as in Fig. 7 but for GW190814.

for (c_{21}, ι), no such bimodality is to be expected, and indeed, the posterior for c_{21} is unimodal. The corresponding Fig. 8 for GW190814 leads to similar conclusions.

V. SUMMARY AND CONCLUSIONS

We have set up a Bayesian analysis framework to test GR by looking at the amplitudes of subdominant modes in GW signals from BBH coalescences, using a state-of-the-art waveform model. Specifically, we allow for modifications in the amplitudes of the (3, 3) and (2, 1) modes, which tend to be the strongest among the subdominant modes. Apart from performing parameter estimation on the associated testing parameters c_{33} and c_{21}, this allows for hypothesis ranking between the presence and absence of such anomalies in the modes.

Results from simulations involving injected waveforms in stationary, Gaussian noise largely follow the trends one would expect based on the dependence of mode amplitudes on total mass and mass ratio: for similar SNRs, heavier and more asymmetric systems make it easier to find violations of GR of the type studied here.

We then performed the first analysis of this kind on the real events GW190412 and GW190814, which were associated with significantly unequal component masses, and in which strong evidence for subdominant mode content had been found [26–28]. Log Bayes factors indicated no evidence for a GR violation in either the (2, 1) or (3, 3) mode. In the case where the (3, 3) mode was being investigated, the posterior density function for c_{33},

while being consistent with the GR value $c_{33} = 0$, did exhibit bimodality, but this was shown to result from correlations between c_{33} and the inclination angle ι. Since the bimodality was also present in c_{33} posterior densities for injections with parameters similar to the ones of GW190412 and GW190814 and $c_{33} \neq 0$, some caution is called for in interpreting such posteriors, at least for BBHs with total mass $M \lesssim 50\ M_{\odot}$. However, our results show that log Bayes factors $\ln \mathcal{B}_{\mathrm{GR}}^{\mathrm{NonGR}}$, which were not considered in previous work in this context [34], are robust indicators for or against the presence of a violation of GR.

Even in systems with significantly asymmetric masses and high total mass, with second-generation detectors, GR violations have to be sizeable ($c_{33} \gtrsim 1.5$ and $c_{21} \gtrsim 3$) in order to be confidently detected. It will be of interest to see how the sensitivity of our method will improve going towards Einstein Telescope [47–50], Cosmic Explorer [50–53], and the space-based LISA [54], but this is left for future work.

[1] J. Aasi *et al.* (LIGO Scientific Collaboration), Classical Quantum Gravity **32,** 074001 (2015).
[2] F. Acernese *et al.* (VIRGO Collaboration), Classical Quantum Gravity **32,** 024001 (2015).
[3] B. Abbott *et al.* (LIGO Scientific, Virgo Collaborations), Phys. Rev. Lett. **116,** 061102 (2016).
[4] B. P. Abbott *et al.* (LIGO Scientific, Virgo Collaborations), Phys. Rev. Lett. **116,** 241103 (2016).
[5] B. P. Abbott *et al.* (LIGO Scientific, Virgo Collaborations), Phys. Rev. X **6,** 041015 (2016); **8,** 039903(E) (2018).
[6] B. P. Abbott *et al.* (LIGO Scientific, Virgo Collaborations), Phys. Rev. X **9,** 031040 (2019).
[7] R. Abbott *et al.* (LIGO Scientific, Virgo Collaborations), Phys. Rev. X **11,** 021053 (2021).
[8] R. Abbott *et al.* (LIGO Scientific, VIRGO, KAGRA Collaborations), arXiv:2111.03606.
[9] B. P. Abbott *et al.* (Virgo, LIGO Scientific Collaborations), Phys. Rev. Lett. **119,** 161101 (2017).
[10] B. P. Abbott *et al.* (LIGO Scientific, Virgo Collaborations), Astrophys. J. Lett. **892,** L3 (2020).
[11] R. Abbott *et al.* (LIGO Scientific, KAGRA, VIRGO Collaborations), Astrophys. J. Lett. **915,** L5 (2021).
[12] B. P. Abbott *et al.* (LIGO Scientific, Virgo Collaborations), Phys. Rev. Lett. **116,** 221101 (2016); **121,** 129902(E) (2018).
[13] B. P. Abbott *et al.* (LIGO Scientific, Virgo Collaborations), Astrophys. J. Lett. **882,** L24 (2019).
[14] B. P. Abbott *et al.* (LIGO Scientific, Virgo Collaborations), Phys. Rev. Lett. **123,** 011102 (2019).
[15] B. P. Abbott *et al.* (LIGO Scientific, Virgo Collaborations), Phys. Rev. D **100,** 104036 (2019).
[16] R. Abbott *et al.* (LIGO Scientific, Virgo Collaborations), Phys. Rev. D **103,** 122002 (2021).
[17] R. Abbott *et al.* (LIGO Scientific, VIRGO, KAGRA Collaborations), arXiv:2112.06861 [Phys. Rev. D (to be published)].
[18] K. G. Arun, B. R. Iyer, M. S. S. Qusailah, and B. S. Sathyaprakash, Classical Quantum Gravity **23,** L37 (2006).
[19] K. G. Arun, B. R. Iyer, M. S. S. Qusailah, and B. S. Sathyaprakash, Phys. Rev. D **74,** 024006 (2006).
[20] N. Yunes and F. Pretorius, Phys. Rev. D **80,** 122003 (2009).
[21] T. G. F. Li, W. Del Pozzo, S. Vitale, C. Van Den Broeck, M. Agathos, J. Veitch, K. Grover, T. Sidery, R. Sturani, and A. Vecchio, Phys. Rev. D **85,** 082003 (2012).
[22] T. G. F. Li, W. Del Pozzo, S. Vitale, C. Van Den Broeck, M. Agathos, J. Veitch, K. Grover, T. Sidery, R. Sturani, and A. Vecchio, J. Phys. Conf. Ser. **363,** 012028 (2012).
[23] M. Agathos, W. Del Pozzo, T. G. F. Li, C. Van Den Broeck, J. Veitch, and S. Vitale, Phys. Rev. D **89,** 082001 (2014).
[24] J. Meidam *et al.*, Phys. Rev. D **97,** 044033 (2018).
[25] L. Blanchet, G. Faye, B. R. Iyer, and S. Sinha, Classical Quantum Gravity **25,** 165003 (2008); **29,** 239501(E) (2012).
[26] R. Abbott *et al.* (LIGO Scientific, Virgo Collaborations), Phys. Rev. D **102,** 043015 (2020).
[27] R. Abbott *et al.* (LIGO Scientific, Virgo Collaborations), Astrophys. J. Lett. **896,** L44 (2020).
[28] S. Roy, A. S. Sengupta, and K. G. Arun, Phys. Rev. D **103,** 064012 (2021).
[29] C. Van Den Broeck and A. S. Sengupta, Classical Quantum Gravity **24,** 155 (2007).
[30] C. Van Den Broeck and A. S. Sengupta, Classical Quantum Gravity **24,** 1089 (2007).
[31] R. Essick and P. Landry, Astrophys. J. **904,** 80 (2020).
[32] I. Tews, P. T. H. Pang, T. Dietrich, M. W. Coughlin, S. Antier, M. Bulla, J. Heinzel, and L. Issa, Astrophys. J. Lett. **908,** L1 (2021).
[33] S. Dhanpal, A. Ghosh, A. K. Mehta, P. Ajith, and B. S. Sathyaprakash, Phys. Rev. D **99,** 104056 (2019).
[34] T. Islam, A. K. Mehta, A. Ghosh, V. Varma, P. Ajith, and B. S. Sathyaprakash, Phys. Rev. D **101,** 024032 (2020).
[35] S. Kastha, A. Gupta, K. G. Arun, B. S. Sathyaprakash, and C. Van Den Broeck, Phys. Rev. D **98,** 124033 (2018).
[36] S. Kastha, A. Gupta, K. G. Arun, B. S. Sathyaprakash, and C. Van Den Broeck, Phys. Rev. D **100,** 044007 (2019).
[37] C. D. Capano and A. H. Nitz, Phys. Rev. D **102,** 124070 (2020).
[38] M. Boyle, L. E. Kidder, S. Ossokine, and H. P. Pfeiffer, arXiv:1409.4431.
[39] L. Blanchet, Living Rev. Relativity **17,** 2 (2014).
[40] G. Pratten *et al.*, Phys. Rev. D **103,** 104056 (2021).
[41] A. Ramos-Buades, P. Schmidt, G. Pratten, and S. Husa, Phys. Rev. D **101,** 103014 (2020).
[42] J. Veitch and A. Vecchio, Phys. Rev. D **81,** 062003 (2010).
[43] H. Jeffreys, *Theory of Probability*, 3rd ed. (Oxford University Press, Oxford, England, 1961).
[44] J. Skilling, Bayesian Anal. **1,** 833 (2006).
[45] J. Veitch *et al.*, Phys. Rev. D **91,** 042003 (2015).

[46] LIGO Scientific Collaboration, LIGO Algorithm Library—LALSuite, free software (GPL) (2018), https://git.ligo.org/lscsoft.

[47] M. Punturo *et al.*, Classical Quantum Gravity **27**, 084007 (2010).

[48] S. Hild *et al.*, Classical Quantum Gravity **28**, 094013 (2011).

[49] M. Maggiore *et al.*, J. Cosmol. Astropart. Phys. 03 (2020) 050.

[50] V. Kalogera *et al.*, arXiv:2111.06990.

[51] B. P. Abbott *et al.* (LIGO Scientific Collaboration), Classical Quantum Gravity **34**, 044001 (2017).

[52] D. Reitze *et al.*, Bull. Am. Astron. Soc. **51**, 035 (2019).

[53] M. Evans *et al.*, arXiv:2109.09882.

[54] S. Babak, A. Petiteau, and M. Hewitson, arXiv:2108.01167.

[55] https://www.gw-openscience.org.